Effects of temperatures and carbon dioxide nanobubbles on superior electric storage for anodically oxidized films of AlY10 amorphous alloy

	Mikio Fukuhara, Tomoyuki Kuroda, Fumihiko Hasegawa, Masayoshi Takahashi, Tomoyuki Suwa, Toshiyuki Hashida, Kazuhisa Sato, Masahiko Nishijima, K Konno
journal or publication title	AIP Advances
volume	9
page range	095202
year	2019-09-05
URL	http://hdl.handle.net/10097/00130705

Mikio Fukuhara, Tomoyuki Kuroda, Fumihiko Hasegawa, Masayoshi Takahashi, Tomoyuki Suwa, Toshiyuki Hashida, Kazuhisa Sato, Masahiko Nishijima, and K. Konno

COLLECTIONS

Paper published as part of the special topic on Chemical Physics, Energy, Fluids and Plasmas, Materials Science and Mathematical Physics

View Online   Export Citation   CrossMark

ARTICLES YOU MAY BE INTERESTED IN

Effects of temperatures and carbon dioxide nanobubbles on superior electric storage for anodically oxidized films of AlY$_{10}$ amorphous alloy

View Online   Export Citation   CrossMark

Mikio Fukuhara,[1,a) ID] Tomoyuki Kuroda,[1] Fumihiko Hasegawa,[1] Masayoshi Takahashi,[1] Tomoyuki Suwa,[1]
Toshiyuki Hashida,[2] Kazuhisa Sato,[2] Masahiko Nishijima,[3 ID] and K. Konno[4]

AFFILIATIONS

[1] New Industry Creation Hatchery Center, Tohoku University, Aoba, Sendai 980-8579, Japan
[2] Fracture and Reliability Research Institute, Graduate School of Engineering, Tohoku University, Sendai 980-8579, Japan
[3] The Electron Microscopy Center, Tohoku University, Aoba, Sendai 980-8577, Japan
[4] National Institute of Technology, Sendai College, Natori 981-1239, Japan

[a)] Corresponding author: Electronic mail: fukuhara@niche.tohoku.ac.jp

ABSTRACT

The effects of temperature and nanometer-sized bubbles (NBs) on a superior electric storage capacitor for anodically oxidized films of AlY$_{10}$ amorphous alloys were determined at temperatures ranging from 275 to 298 K in 0.4 M H$_2$SO$_4$ solutions with NBs of ozone, oxygen, and carbon dioxide. The AAO specimen obtained by solution with carbon dioxide NBs at 278 K showed longer discharging time. The discharging time increases with increasing charging time and then saturates after around 70 s. The increment in temperature makes the structure from simple series capacitor with large capacitance to simple parallel capacitor with lower capacitance and larger resistance. The stability of NBs in water could be explained by enclosure in protonated polyhedral water clusters. The collapse of clusters with oxygen NBs result in the formation of OH$^-$ radicals and its resulting elution of Al, while carbon oxide NBs prevent the formation of OH$^-$ radicals, promoting sluggish oxidation that is required for the formation of AlO$_6$ clusters.

I. INTRODUCTION

Storage of electrical energy is currently attracting a great deal of interest in the field of physics.[1–6] A significant amount of attention has been given to power source devices such as batteries and fuel cells. The current electrochemical capacitor is an electric double-layer capacitor (EDLC) where the porous interfaces of high specific-area carbon materials are charged and discharged by ion or radical diffusion in liquid electrolytic solutions.[3,5,6] The fractal structure of an EDLC is composed of a distributed constant equivalent circuit of active carbon (R) and electrolyte (C). Recently, we found that amorphous titanium-oxides (golden, a-TiO$_{2-x}$, ATO)[7,8] and aluminum-oxides (blackish, a–Al$_2$O$_{3-y}$, AAO), showing an RC constant larger

than EDLC and switching effect of positive and negative electricity from the atmosphere,[9] respectively, can be regarded as a superior electric storage device with nanometer-sized uneven surfaces.[10,11] Thus, we can apply rechargeable dry supercapacitors in place of practical Li ions. We termed this device a "dry" electric distributed constant capacitor (EDCC). Since the electric capacitance of these amorphous surfaces increases proportionally to the negative sixth power of the convex diameter up to 7 mF/cm^2, we must investigate effective method on fabrication of AAO with uneven surfaces below 30 nm.

In this study, we report effects of temperatures and nanometer-sized bubbles (NBs) on anodic oxidization conditions for AAO coated AlY$_{10}$ alloy supercapacitors in sulfuric acid solutions,

intending to obtain further higher capacitances by miniatuarization of convex diameter. Anodic oxidation process provides self-organized fine structures for electronic, optical and microchemical devices.[12,13] However, little research about anodically oxidized aluminum oxides for supercooled amorphous alloys have been performed. AAO is an attractive material for electronic applications such as dielectrics,[14,15] capacitors,[16,17] and photoluminescence.[18] Tavakoli et al.[19] have reported that AAO with a surface area greater than 370 m^2/g is the most energetically stable phase. Our results showed that insulating blackish AAO with nanometer-sized roughness provides an ideal candidate for supercapacitors with various electrical applications.[9,11] Anodization of amorphous aluminum alloys can produce uneven AAO layer with lower aspect ratios that cannot be realized by using crystalline aluminum.[9,13]

On the other hand, much attention has been devoted to examining the various effects of oxygen, hydrogen, nitrogen, and ozone NBs in water for medical, biological, agricultural, fishing, and environmental applications.[20–24] The NB has come into light recently as a bubble with a size distribution of less than 100 nm.[20,24] Although gas bubbles over micron size cannot live long in water, NBs have a half-collapsing time of several days.[24] Herein, we present the effects of three types of NBs on a superior electric storage capacitor for anodically oxidized films of Al-Y amorphous alloy ribbons in sulfuric acid solutions. Although the use of ozone NBs accelerates the formation of 2-10 nm-size oxide films for Ti-Ni-Si amorphous alloy ribbons at lower than 10 V,[25] the effect of ozone NBs for AlY$_{10}$ amorphous alloy have not been investigated yet.

II. EXPERIMENTAL

Amorphous alloy AlY$_{10}$ (nominal compositions) ribbons with width of about 3-5 mm and thickness of about 50 μm were prepared in helium atmosphere from argon arc-melted ingots using the rotating wheel method.[9,11] The blackish AAO specimens were prepared by using the anodic polarization process in 0.4 mol H$_2$SO$_4$ solution at 275, 278, 283, 288 and 293 K, and 16 V, with AlY$_{10}$ alloy ribbons under air bubbling of 10 cc/s, using platinum counter electrodes. NB waters were prepared by dispersing micronized bubbles of the targeted gas in aqueous solutions for more than ten minutes. Because the zeta potential measurements showed that the NBs were negatively charged within the given range of pH and that a higher electrical charge was observed in oxygen NBs,[26] we used oxygen, ozone, and carbon dioxide NBs as the oxidization solvents. The bubble size was measured by Dynamic Light Scattering (DLS) (FDL-300, Otsuka Electronics). Solute content was analyzed by gas chromatography-mass spectroscopy (GCMS-QP2010,

Shimadzu). Table I lists the bubble size, solute content, and color for water with oxygen, ozone, and carbon dioxide NBs. Sample structure was examined by X-ray diffraction (XRD-7000X, Shimadzu). The surface morphologies were analyzed by atomic force microscope (AFM: SPA400 SII Nano Technology) using a tapping scan mode for a scanning window of 0.5 × 0.5 μm^2 with 512^x × 256^y measurement points. After preparing TEM specimen by Focused Ion Beam (FIB; Quanta 3D Dual Beam system, Thermo Fisher Scientific) using lift-out method, depth of layers was determined from elemental mapping of Al, Y, and O by Scanning Transmission Electron Microscope (STEM) with an aberration-corrected TEM (Titan^3 G2 60-300 Probe Corrector, Thermo Fisher Scientific) at 200 kV.

The specimen was sandwiched directly by two copper ribbons beneath two pieces of glass plates using a clamp. The charging/discharging behavior of the specimen was analyzed using the galvanostatic charge/discharge on a potentiostat/galvanostat (SP-150, BioLogic Science) with dc of 10 V and current in the range from 1 pA to 1 mA for ~600 s at room temperature, with a complex impedance between 1 mHz and 1 MHz and 10 mV.

III. RESULTS

A. Effects of NBs on discharging energy for anodic oxidization

To investigate the effects of NBs on the anodic oxidation of amorphous alloys, we studied the oxidation behaviors for the alloys in four types of 0.4 M H$_2$SO$_4$ solutions: pure water and water solutions with oxygen (9.78 mg/l), ozone (2 mg/l) and carbon dioxide (50 mg/l) NBs. Since the alloy was completely eluded into ozone NBs during anodization, we could not use the ozone one. The current density-time curves during the potentiostatic polarization at 16 V and 278 K for the H$_2$SO$_4$ solutions with pure water, and oxygen and carbon dioxide NBs are shown in Fig. 1(a). All curves show an abrupt increase at the beginning of oxidization and then reach the peaks, and finally gradually decrease down to zero current. The current densities stand in order of peak values of oxygen NBs, pure water, and carbon dioxide NBs, but the half width of the peaks is carbon dioxide, oxygen NBW and pure water in order. All specimens were blackish. The charging and discharging behaviors under a constant current at 1 nA after charging at 10 V for 50 s at a direct current (DC) of 1 mA is shown in Fig. 1(b), indicating long and short discharging times for carbon dioxide and oxygen NBWs solutions, respectively, compared with pure water used in the previous papers.[9,11] We observed the same results for repeated tests. Therefore, we selected carbon dioxide NBs as solvent of H$_2$SO$_4$ solution in the next section.

TABLE I. Bubble size, solute content and color for water with ozone, oxygen and carbon dioxide NBs.

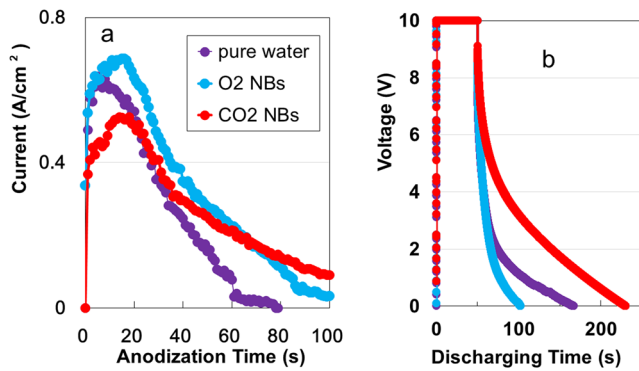| NB water	Bubble size	Solute content	Color
2 mg/l ozone	< 100 nm	0.1 mass% Na, < 1ppm Mn	pink
9.78 mg/l oxygen	< 100 nm	0.05 mass% Na	transparent
50 mg/l carbon dioxide	< 100 nm	0.05 mass% Na	transparent

FIG. 1. Current-time curves for 100 s during anodization (a), and charging and discharging behaviors (b) for voltage of AAO specimens anodically oxidized for 61, 74 and 67 s, respectively, at 16 V and 278 K in 0.4 M H_2SO_4 solutions using three kinds of solvents containing of pure water, and water with oxygen (9.78 mg/l) and carbon dioxide (50 mg/l) NBs.

FIG. 3. (a) Relation between discharging (stored) energy for a constant DC of 1nA and anodization time (energy) for the fabrication of AAO. (b) Charging and discharging behaviors for voltage of AAO specimens anodically oxidized at 16 V, and at 275, 278, 283, 288 and 293 K for 35, 67, 20, 35 and 42 s, respectively, in 0.4 M H_2SO_4 solutions with carbon dioxide (50 mg/l) NBs.

B. Effects of temperature on discharging energy for anodic oxidization

Next we carried out anodic oxidization of AlY_{10} amorphous alloys at 16 V and 275, 278, 283, 288, and 293 K in 0.4 M H_2SO_4 solutions with carbon dioxide NBs. The temperature dependent current density-time curves are shown in Fig. 2(a). The increase in temperature raises the peak current and decreases the half width of the curves (Fig. 2(b)). The discharging behavior under the same condition as Fig. 1(b) is presented in Fig. 3(a) for the AAO samples anodically oxidized at 16 V, and at 275, 278, 283, 288 and 293 K for 35, 67, 20, 35 and 42 s, respectively. The discharging curves are linear curves typical for conventional supercapacitors. This can be explained by electroadsorption[27] occurring on nanometer-sized capacitors. The discharging ones at 278 K continued up to 229 s. The discharging (stored) energies obtained from the integrated area (voltage × time) in all voltage-discharging time diagrams are shown in Fig. 3(b), as a function of anodization time. All curves display similar patterns with peaks at (27-49) s. The temperature dependence of stored energy
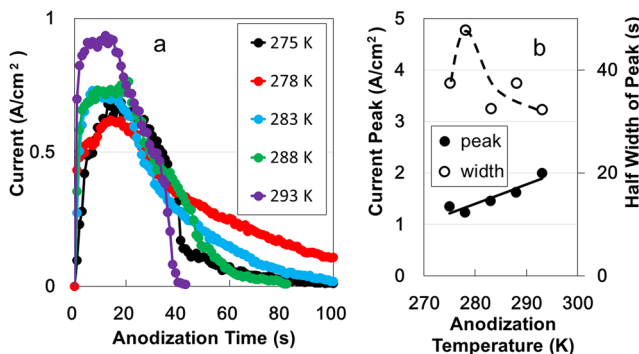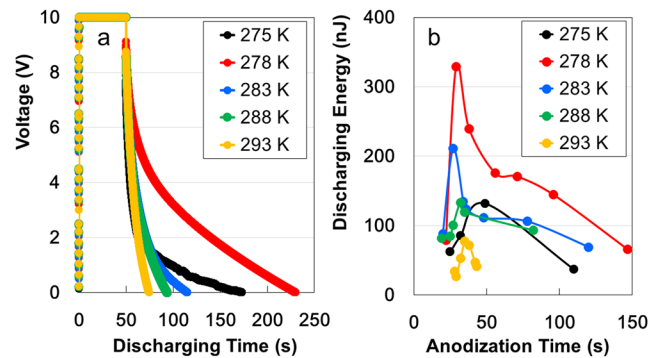
demonstrates that the stored energy at 278 K is around four times larger than that of 293 K.

C. Complex electric evaluation on temperature for electric storage

To non-destructively analyze the electrostatic contribution of the specimen for electric storage, we measured the AC (alternate current) impedance from 1 mHz to 1 MHz in Nyquist and Bode diagrams at room temperature. The Nyquist (complex impedance plane) plot for the specimen is shown in Fig. 4a. The specimen's variation in impedance with frequency followed the three kinds of combined patterns, a straight line along a nearly vertical line for 278 K, a semicircle and a straight line for 275 and 283 K, a line with slope of π/4 rad and a semicircle for 288 and 293 K. The impedance data at 278 K fits a nearly vertical line, as produced by a series RC circuit, which is similar to a graphene EDLC.[28] The π/4 rad region (Warburg region) is known as a consequence of the distributed resistance/capacitance in the porous electrode.[17,29] Thus the electric structures on AAO specimens are divided broadly into three categories; simple series capacitor with large capacitance at 278 K, the simple parallel capacitor with relatively small capacitance and larger resistance at 275 and 283 K, and the simple parallel capacitor with lowest capacitance and largest resistance at 283 and 293 K. As a result, the capacitance decreases and resistance increases, as temperature increases. This can be proved by the enhancement of real impedance at 275 and 293 K in Fig. 4(b) and imaginary impedance at 275 and 278 K in Fig. 4(c) in the lower-frequency region of the Bode diagram. The decrement to −90° in phase angle with decreasing frequency at 278 K is evidence of DC charging (Fig. 4(d)). There is a possibility that the specimen obtained at 275 K also reveals DC charging. The increment of temperature makes the structure from simple series to simple parallel circuit, as can be seen from increasing up to 0° in phase angle. Figure 5(a) and (b) show the frequency-dependent series Cs and parallel Cp capacitances, respectively, as a function of temperature. Cs is twice larger than Cp for all temperatures in the lower-frequency region. Since experimental equations (1 mHz < f < 1 Hz) of Cs curve at 278 K can be expressed as $Cs = 10^{-5}f^{-1.128}$ ($r^2 = 0.9982$), where f is the frequency, DC capacitance

FIG. 2. (a) Current-time curves during anodization at 16 V, and at 275, 278, 283, 288 and 293 K for 100 s in 0.4 M H_2SO_4 solutions with carbon dioxide (50 mg/l) NBs. (b) Anodization temperature effect on maximum current and half width of the peak.
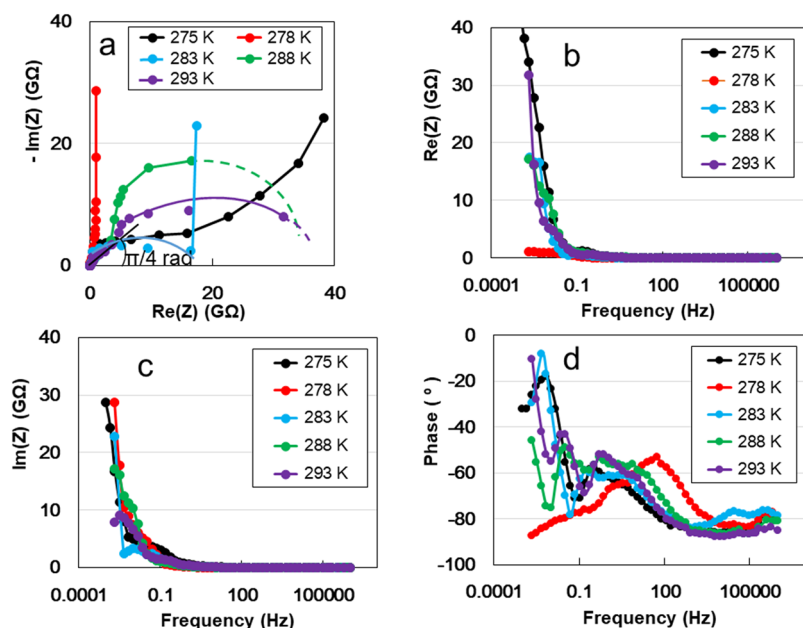
FIG. 4. Nyquist plot (a), Bode plots for the real (b) and imaginary (c) impedances, and phase angle (d) as a function of frequency for AAO specimens anodically oxidized at 16 V, and at 275, 278, 283, 288 and 293 K for 35, 67, 20, 35 and 42 s, respectively, in 0.4 M H_2SO_4 solutions with carbon dioxide (50 mg/l) NBs.

could be increased considerably. Thus temperature plays an active role in enhancement of capacitance.

D. Surface characterization for electric storage

Then, we observed the surface characteristics of two representative AAO specimens anodized at 278 and 293 K. Figures 6(a) and (b) show the atomic force microscope (AFM) images for two specimens, respectively. These figures, which are similar to those previously reported for ATO[10] and amorphous perfluoroalkenyl vinyl ether polymer (APP),[30] reveal spots with a convexity of 25 (c) and 113 (d) nm and a concavity of 17.5 (c) and 152 (d) nm in diameter, respectively. Thus, it shows that the increase in temperature promotes rough unevenness. The morphological effect for superior electron storage will be addressed in subsequent paper. From High
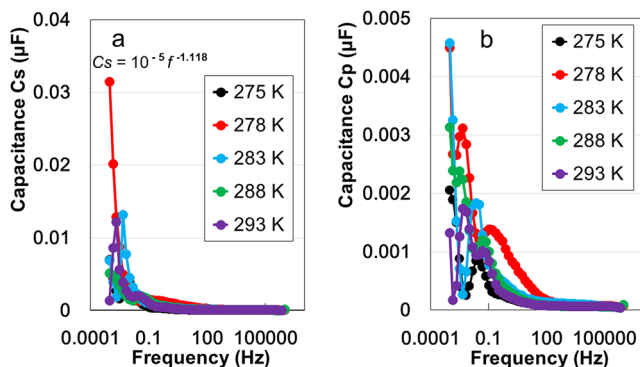

FIG. 5. Relation between series (a) and parallel (b) capacitances and frequency for AAO specimens anodically oxidized at 16 V, and at 275, 278, 283, 288 and 293 K for 35, 67, 20, 35 and 42 s, respectively, in 0.4 M H_2SO_4 solutions with carbon dioxide (50 mg/l) NBs.

angle Annular Dark-Field Scanning TEM (HAADF-STEM) image (Fig. 6e) and elemental mapping of Al, Y, and O in Fig. 6 (f), (g), (h), respectively, we observed a thick aluminum oxide layer with 15 μm in depth on the AlY_{10} alloy. The formation rate was calculated as 0.177 mm^3/s, which is around forty thousand times larger than that (4.3×10^{-6} mm^3/s)[7] of ATO with passive oxide films. The larger formation rate would be responsible for superior electric storage for blackish amorphous aluminum oxide specimens with the nanometer-sized uneven surface.

E. Effect of repeated charging time and RC constant evaluation for electric storage

Lastly, we determined an effect of repeated charging time and RC constant evaluation for electric storage. The rapid decrease in voltage at the beginning of discharging in Fig. 1(b) and Fig. 3(a) is analogous to an ohmic *IR* drop in EDLCs.[31] If the decrease is *IR* drop, the potential drop is caused by current passing through resistive elements for internal charging of unsaturated cells in an equipment circuit of the matrix.[32] To make clear the drop behavior, we investigated the integrated charging by repeated charging. Fig. 7(a) shows discharging behaviors under a constant current of 1 nA after charging for 1, 60, and 120 s at 10 V. The discharging time increases with increasing charging time and then saturates after around 70 s (inset of Fig. 7a). This indicates *IR* drop, which is characteristic of EDCCs with electric distributed constant circuits.[11]

It is crucial to evaluate *RC* constant for practical use of the dry EDCCs. Figure 7(b) shows a frequency dependent *RC* constant in the input voltage of 10 V at room temperature. *RCs* increase parabolically from around 0.1μs to around 1.4 ks with decreasing frequency. In *RCs*, 1,424 s at 1 mHz is 285 thousand times larger than that (5 ms) in the conventional EDLC.[32] Larger *RCs* from 0.1 s to a few hours is required for practical use.
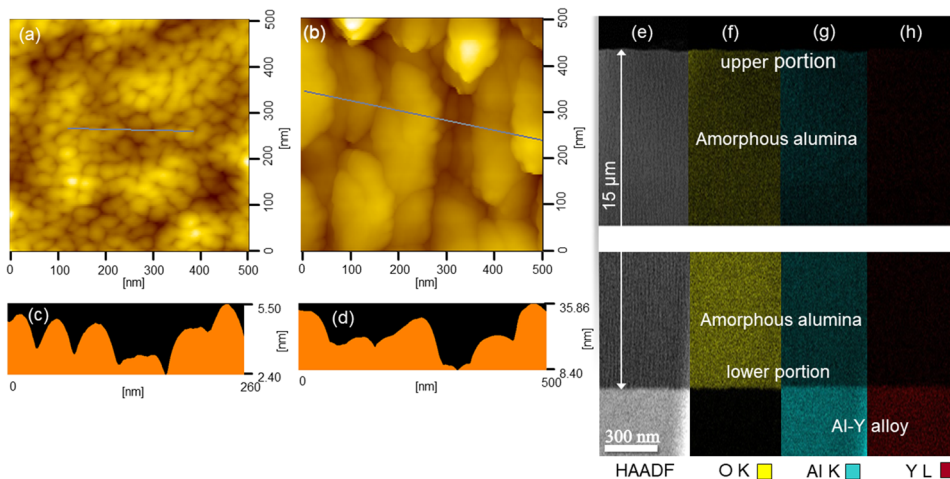
FIG. 6. AFM images for surfaces of specimens anodically oxidized at 278 (a) and 298 K (b), respectively. Height profiles (c) and (d) correspond to grey lines in upper images (a) and (b), respectively. HAADF-STEM image (e) and mapping profiles of Al (f), Y (g), and O (h) for the cross section of specimens anodically oxidized at 278 K.

IV. DISCUSSION

Although we lay our hopes on engineering application of NBs, in our knowledge, there are no reports except for effective application of ozone NBs.[25] In this study, we reported that the specimen anodized by carbon dioxide NBs showed superior electric storage. However, it is not clear yet why NBs can stay in water for a long time and carbon oxide NBs provide the practical anodization effect. We first consider a stabilization mechanism of NBs in water.

Formation of neutral clusters such as $(H_2O)n$ has been practically limited to n values up to ten,[33,34] but Mizuse et al.[35] reported that hydrogen-bonded network structures form close net (multiple rings) structures with large protonated water clusters $H^+ (H_2O)n$ (n = 20-200).[33] We here propose a mechanism that the large protonated water clusters can include oxygen and carbon dioxide NBs. We then calculate diameters of inscribed spheres and number of molecules for oxygen and carbon dioxide NBs, as a function of the number of polyhedron cluster face, although Chaplin[36] has simulated to n

values up to 280 alone, provided that the regular polyhedron cluster inscribes true sphere of these NBs. As it can be seen from Fig. 8a, the diameter first increases parabolically and then saturates as the number of the cluster face increases. By contrast, the number of molecules increases linearly with an increase in the number of the cluster face. Maheshwary et al.[37] reported that the most energetically stable geometries for water clusters arise from the fusion of tetrameric or pentameric rings, i.e., cuboids and fused pentameric structures. In these cases, both diameters of the inscribed sphere and number of molecules are smaller than those of the regular polyhedron cluster.

Our next interest lies in studying the electrostatic potential of oxygen atoms with nanometer-sized convex in oxygen and carbon dioxide NBs by the help of the quantum-size effect according to the Thomas-Fermi (TF) electronic screening theory. The TF model has been applied to approximate calculations of potential fields and charge densities in elements as a function of molecular spacing. To the best of our knowledge, however, no detailed investigation has been conducted into the quantum-size effect for the electrostatic potential of NBs.

From Eqs. (S5) and (S8) in supplementary material, we can calculate the electrostatic potential and the induced outer electronic pressure of the oxygen atoms consisting of the oxygen and carbon dioxide NBs, using the ionic oxygen radius of 0.140 (Ref. 38) and 0.105 (=0.1163 (carbon-oxygen bond length, Ref. 39)×0.140/(0.140+0.015 (radius of carbon, Ref. 38))) nm, respectively. As the carbon dioxide molecules are linear and centosymmetric in covalent nature, its oxygen radius is shorter than that of oxygen molecule. These results are presented in Fig. 8a for oxygen and Fig. 8b for carbon dioxide NBs, respectively. The carbon dioxide NB in a water cluster is more electrostatically stable than that of oxygen ones. The decrease in bubble diameter increases the negative electrostatic potential and positive electron pressure. Stability of both the NBs increase further as the bubble diameter decreases, i.e., the pressure increases, due to protonated water clusters with positive charges. However, when the electron pressure is small, the hydrated proton pressure destroys an H-bond, which is due to an intermolecular cluster attraction between the hydrogen atom of one
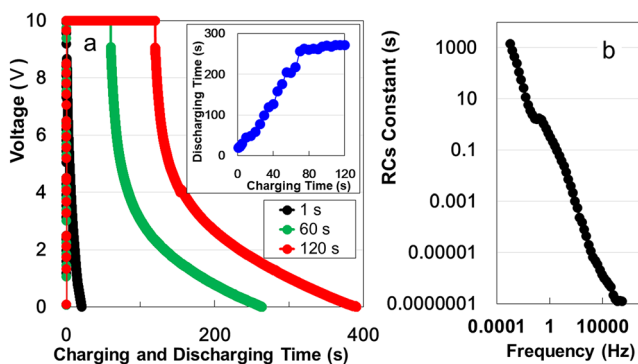

FIG. 7. Charging time dependence of charging and discharging time after 1 mA-10 V charging (a) and frequency dependence of RC constant in put voltage of 10 V at room temperature (b) for AAO specimens anodically oxidized at 16 V and 278 K for 67 s in 0.4 M H_2SO_4 solutions with carbon dioxide (50 mg/l) NBs. Inset of (a): The charging time dependence of the discharging time.
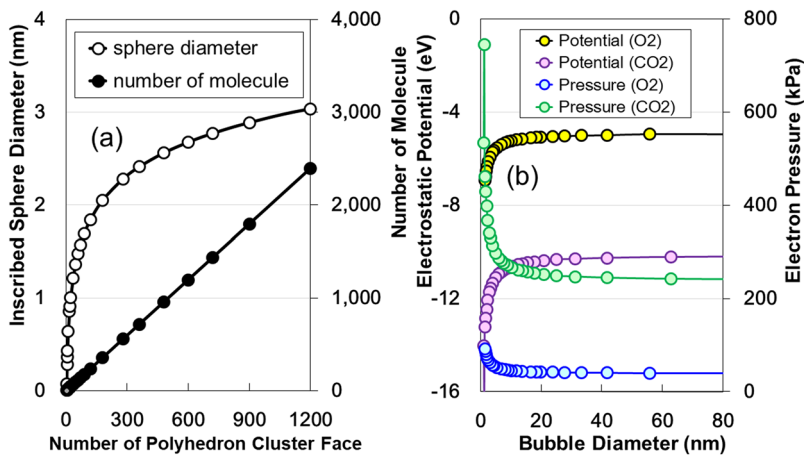
FIG. 8. (a) Diameter of inscribed sphere and number of molecules for oxygen and carbon dioxide NBs, as a function of the number of polyhedron cluster faces. (b) Bubble diameter dependence of the electrostatic potential and electron pressure for oxygen ions of the oxygen and carbon dioxide NBs.

water molecule and the lone-pair electrons on another,[40] leading to a collapse of the water clusters.[41] Thus, there is a critical size for stabilization of NBs.

According to the formation mechanism of anodic alumina films,[42] anodization of Al in H_2SO_4 solution is carried out by electrochemical oxidization of Al substances in water through two different routes: an electrolytic reaction of water, which accelerate increment of hydroxide ions OH^- by addition of H_2SO_4,
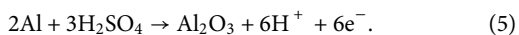
$$H_2O \rightarrow 2H^+ + O^{2-} \tag{1}$$

$$\rightarrow H^+ + OH^-, \tag{2}$$

and through the solution of Al electrode into the solution, *i.e.*, the formation of Al^{3+} ions.

$$Al \rightarrow Al^{3+} + 3e^- \tag{3}$$

The anodic oxide film formation at the barrier layer is determined through the migration of O^{2-} anions to the metallic aluminum surface.

$$2Al^{3+} + 3O^{2-} \rightarrow Al_2O_3. \tag{4}$$
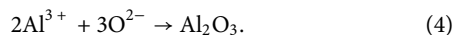
As a result, the following overall oxidation reaction occurs

$$2Al + 3H_2SO_4 \rightarrow Al_2O_3 + 6H^+ + 6e^-. \tag{5}$$

For the H_2O solution with ozone NBs, the ozone NBs provide the most effective oxidant, OH^-, owing to free-radical generation under strong acidic conditions.[42] The hydroxide ions form water-soluble tetrahydroxyaluminate ions, leading to complete elution of Al.

$$2Al + 10H_2O + 2OH^- \rightarrow 2[Al(OH)_4(H_2O)_2]^- + 3H_2 \tag{6}$$
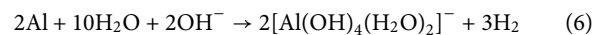
Thus, we could not use the ozone NBs in this study.

We next consider the effect of oxygen and carbon dioxide NBs. Here, it should be noted that Takahashi and Chiba[20] showed that free-hydroxyl (OH) radicals formed during the collapse of ozone microbubbles play an important role for induction of chemical reactions that lead to the decomposition of organic chemicals such as sterilization. Hence, by analogy, we infer that two similar hydroxyl radicals (˙OH) generated during collapse of protonated water clusters $H^+ (H_2O)n$ for oxygen NBs, by combination of H from the clusters and O separated from the NBs (Fig. 9a), leading to partial elution of Al, as can be seen from the current density-time curves at the beginning of anodization in Fig. 1(a). However, the anodic film formation at the barrier layer takes precedence of the solution after around 20 seconds. As can be seen from Fig. 1a, conversely, the current density curve of carbon dioxide NBs reveals lower peak and longer half width of the curve in comparison with
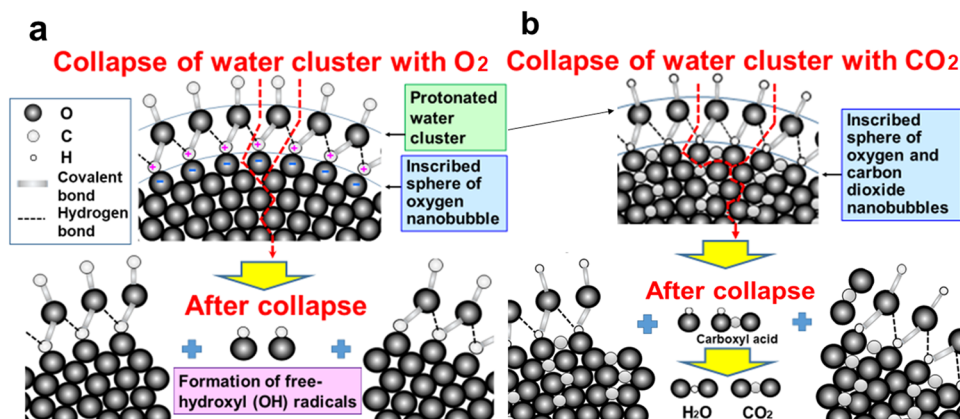

FIG. 9. Collapse of protonated water clusters with inscribed spheres of oxygen and carbon dioxide NBs and formation of two hydroxyl radicals (˙OH) (a) and H_2O and CO_2 (b).

H_2SO_4 solutions with pure water and ozone NBs. Figure 9(b) suggests that Brønsted acid (carboxylic acid, COOH)[43] reacts immediately with other surrounding OH^- formed by addition of H_2SO_4 to make H_2O and CO_2 molecules after polyhedral water clusters filled with NBs were broken. The H_2O molecule remains in water solution, but the CO_2 molecule rises to the surface of the solution. As a result, it is expected that the solution rate of Al in carbon dioxide NBs becomes slower compared with H_2SO_4 solutions with pure water and oxygen NBs, leading to longer oxidation time due to the relative increase of O^{2-} ions. Thus we can conclude that such sluggish formation of AAO by the usage of carbon dioxide NBs is desirable for the formation of AlO_6 clusters with superior electric storage performance.[9] However, because it is currently difficult to draw reliable conclusions as to the precise role of carbon dioxide itself in the present study, further work in this pioneering area is recommended. Furthermore, the air bubbling in H_2SO_4 solution is effective for breaking of water clusters filled with carbon dioxide NBs in addition to the formation of uniform line-field of electric force.

We finally consider the temperature effect on anodization. As can be seen from AFM images of Fig. 6, the oxide surfaces anodized at 293 K showed crude uneven structures in comparison with that at 275 K. As can be seen from long-term anodization[9,11] at 278 K, exothermal reactions in the temperature over 278 K could accelerate the conversion from AlO_6 octahedron to AlO_5 hexahedron or AlO_4 tetrahedron with the lowest storage. On the other hand, anodization at 275 K would prevent from the formation of uniform oxide films by disturbance of line field of electric force caused by the solidification of water within the limit of ±2 K. Thus we selected 278 K as a suitable temperature. Yoshimoto et al.[44] have reported that hardness of the film anodized at 278 K is higher than that obtained at 293 K.

V. CONCLUSIONS

Amorphous AlY_{10} alloy, prepared by the rotating wheel method were anodically oxizized in 0.4 M H_2SO_4 solution with ozone, oxygen, and carbon dioxide NBs for 100 s at 16 V and 275, 278, 283, 288, and 293 K. Stabilization of NB gases in protonated polyhedral water clusters was elucidated with the help of the quantum-size effect according to the Thomas-Fermi electronic screening theory. When the clusters filled with NBs were broken, oxygen NBs generated OH^- radicals, accelerating elution of Al, while carbon oxide NBs prevented the formation of OH^- radicals, promoting sluggish oxidization that is required for the formation of AlO_6 clusters. Anodization at 278 K in carbon dioxide NBs showed superior electric storage for blackish amorphous aluminum-oxide specimens with the nanometer-sized uneven surface with the convexity of 25 nm and concavity of 17.5 nm. The increase in temperature promotes rough unevenness, resulting in conversion from a simple series capacitor with large capacitance to a simple parallel capacitor with lower capacitance and larger resistance.

SUPPLEMENTARY MATERIAL

See supplementary material for methods of electrostatic potential and the electronic pressure of the oxygen atoms of oxygen and carbon dioxide NBs with nonometer-sized convex.

REFERENCES

[1] M. Winter and R. J. Brodd, Chem. Rev. **104**, 4245 (2004).
[2] M. Whittingham, MRS Bull. **33**, 411 (2008).
[3] B. E. Conway, *Electrochemical Supercapacitors: Scientific Fundamentals and Technological Applications* (Plenum Press, New York, 1999).
[4] P. Simon and Y. Gogotsi, Nature Mat. **7**, 845 (2008).
[5] A. S. Aricó, P. Bruce, B. Scrosativ, J. M. Tarascon, and W. Schalkwijk, Nature Mat. **4**, 366 (2005).
[6] M. F. El-Kady, V. Strong, S. Dubin, and R. B. Kaner, Science **335**, 1326 (2012).
[7] M. Fukuhara, H. Yoshida, M. Sato, K. Sugawara, T. Takeuchi, I. Seki, and T. Sueyoshi, Phys. Stat. Sol. RRL **7**, 477 (2013).
[8] M. Fukuhara and K. Sugawara, Nanoscale Res. Lett. **9**, 253 (2014).
[9] M. Fukuhara, T. Kuroda, F. Hasegawa, T. Hashida, E. Kwon, and K. Konno, Europhys. Lett. **123**, 58004 (2018).
[10] M. Fukuhara, T. Kuroda, and F. Hasegawa, Sci. Rep. **6**, 35870 (2016).
[11] M. Fukuhara, T. Kuroda, F. Hasegawa, Y. Shirai, T. Hashida, and K. Konno, J. Alloy. Comp. **776**, 757 (2019).
[12] C. A. Foss, Jr., G. L. Hornyak, J. A. Stockert, and C. R. Martin, J. Phys. Chem. **96**, 7497 (1992).
[13] H. Masuda and K. Fukuda, Science **268**, 1466 (1995).
[14] G. D. Wilk, R. M. Wallace, and J. M. Anthony, J. Appl. Phys. **89**, 5243 (2001).
[15] P. Katiyar, C. Jin, and R. J. Narayan, Acta Mater. **53**, 2617 (2005).
[16] A. I. Mardare, M. Katltenbrunner, N. S. Sariciftci, S. Bauer, and A. W. Hassel, Phys. Stat. Sol. A. **209**, 813 (2012).
[17] R. Kötz and M. Carlen, Electrochim. Acta **45**, 2483 (2000).
[18] G. G. Khan, A. K. Singh, and K. Mandal, J. Lumin. **134**, 772 (2013).
[19] A. H. Tavakoli, P. S. Maram, S. J. Widgeon, J. Rufner, K. van Bethem, S. Ushkov, S. Sen, and A. Navrotsky, J. Phys. Chem. C **117**, 17123 (2013).
[20] M. Takahashi, K. Chiba, and P. Li, J. Phys. Chem. B **111**(39), 11443 (2007).
[21] S. Liu, Y. Otsuka, Y. Makino, and S. Oshita, "Effects of the water containing nanobubbles on metabolic activities of barley seeds," in Proc. 6th Int. Symp. Machinery Mechatronics for Agriculture and Biosystems Eng. (ISMAB) (Jeonju, Korea, 2012), pp. 446−451.
[22] A. Vashita and S. Nagarajan, Ind. J. Biochem. Biophys. **47**, 311 (2010).
[23] J. S. Park and K. Kurata, HortTechnology **19**, 212 (2009).
[24] M. Takahashi, Nanobubbles: An Introduction, in H. Tsuge (Ed.), *Micro-and Nanobubbles: Fundamentals and Applications* (Pan Stanford Publishing Pte, Ltd., Singapore, 2014), pp. 307−315.
[25] M. Fukuhara, T. Kuroda, F. Hasegawa, and K. Chiba, J. Non-Cryst. Sol. **473**, 147 (2017).
[26] M. Takahashi, J. Phys. Chem., B **109**, 21858 (2005).
[27] M. Dupevrat and E. Nakache, J. Colloid Interface Sci. **73**, 332 (1980).
[28] J. R. Miller, R. A. Outlaw, and B. C. Holloway, Science **329**, 1637 (2010).
[29] M. Itagaki, *Electrochemistry, Impedance Method*, 2nd ed. (Maruzen, Tokyo, 2014), p. 93.
[30] M. Fukuhara, T. Kuroda, F. Hasegawa, and T. Sueyoshi, Sci. Rep. **6**, 22012 (2016).
[31] M. Okamura, *Electric Double Layer Capacitor and Its Storage System* (Nikkan Kogyo, Tokyo, 2011), p. 77.
[32] M. Okamura, Transistor Technol. **4**(9), 343 (2001) (in Japanese).
[33] D. Eisenberg and W. Kauzmann, *The structure and properties of water* (Oxford at the Clarendon Press, London, 1969).
[34] U. Buck and F. Huisken, Chem. Rev. **100**, 3863 (2000).

[35] K. Mizuse, N. Mikami, and A. Fujii, Angew. Chem., Int. Ed. **49**, 10119 (2010).

[36] M. F. Chaplin, Biophys. Chem. **83**, 211 (1999).

[37] S. Maheshwary, N. Patel, N. Sathyamurthy, A. D. Kulkarni, and R. Gadre, J. Phys. Chem. **105**, 10525 (2001).

[38] C. Kittel, *Introduction to Solid State Physics*, 4th ed. (John Wiley & Sons, 1971), p. 76.

[39] N. N. Greewood and A. Earnshaw, *Chemistry of the Elements*, 2nd ed. (Butterworth-Henemann), ISBN 0-08-037941-9.

[40] R. Ludwig, Angew. Chem., Int. Ed. **40**, 1808 (2001).

[41] M. Fukuhara and A. Kokuta, CryoLetters **26**, 251 (2005).

[42] V. F. Henley, *Anodic Oxidation of Aluminium and its Alloys* (Pergamon Press, Oxford, 1982).

[43] R. H. Petrucci, W. S. Harwood, and F. G. Herring, *General Chemistry*, 8th ed. (Prentice-Hall, 2002), p. 666.

[44] M. Yoshimoto, Y. Morizono, S. Tsurekawa, and T. Baba, J. Cerm. Soc. Jpn. **120**, 276 (2012).